Materials Advances

ROYAL SOCIETY OF CHEMISTRY

REVIEW

View Article Online
View Journal | View Issue

Cite this: *Mater. Adv.*, 2022, 3, 3726

Recent trends of contrast agents in ultrasound imaging: a review of the classifications and applications

Ali Tarighatnia,[abc] Mohammad Reza Fouladi,[c] Nader D. Nader,[d] Ayuob Aghanejad *[a] and Hossein Ghadiri*[bc]

Ultrasound (US) imaging, due to its capabilities of real-time imaging, portability, low cost and favorable safety, is frequently used as a diagnostic modality for the visualization of different diseases. US imaging is currently the first step in estimating the severity of oncological diseases, cardiovascular conditions, and for accurate assessment and diagnosis. Novel contrast agents have propelled US imaging into a new realm in the cellular and molecular fields and improved its sensitivity and specificity for detecting earlier stages of diseases. Selecting nanoparticles with appropriate structure and performance and a promising feature of binding to the target is a powerful strategy for the targeted imaging and early detection of disease. Here, we update the classification of the most attractive ultrasound contrast agents (USCAs), especially with regards to their advantages and disadvantages for application in US imaging. We also discuss how various technical detection modes of ultrasound imaging and quantitative analysis are affected by disease diagnosis. The clinical translations of US diagnostic strategies have prompted us to explore nanoparticle-based USCAs against various diseases. We also looked into the applications of USCAs in the diagnosis of cardiovascular disorders and oncological diseases based on anatomical section classification.

Received 19th October 2021,
Accepted 28th March 2022

DOI: 10.1039/d1ma00969a

rsc.li/materials-advances

1. Introduction

Diagnostic imaging tasks are the first step in estimating the severity of a disease and for making an accurate assessment. The late diagnosis of malignant diseases and heart problems can lead to increased cost of cancer care and higher mortality rate.[1] Different types of imaging modalities (*e.g.*, positron emission tomography (PET), single-photon emission computed tomography (SPECT), magnetic resonance imaging (MRI), computed tomography (CT), and US) have been used for the early detection of diseases in the clinical setting.[2,3] In this regard, one of the frequently used imaging modalities that can evaluate both cardiovascular diseases and oncologic conditions is ultrasound (US) imaging.[4–6] Among the different imaging modalities, US imaging has assumed a critical role compared to the other modalities due to its real-time and portable imaging capabilities. As a low-cost method with good safety (non-ionizing radiation) and due to its non-invasive and highly penetrating nature, it is more frequently used compared to the other modalities.[7,8]

In US imaging, ultrasound waves propagate through different tissue interfaces. Depending on the acoustic impedance changes between interfaces, the intensity of the produced echoes from the boundaries of structures and from the underlying texture will change.[9] However, while US imaging has a crucial role in assessing the extent of cancer lesions and cardiovascular pathologies, this technique cannot detect the diseases at early stages. In this regard, US imaging using nanoparticles (NPs) as contrast agents can provide early-stage diagnosis and improve imaging sensitivity and specificity. Moreover, US contrast imaging optimizes therapeutic strategies and reduces the mortality rate and the cost of care.[10]

Technically, ultrasound contrast agents (USCAs) increase the difference in acoustic impedance between tissues or within vascular/tissue interfaces, enhancing the reflected acoustic echoes. The acceptance criteria for USCAs are excellent acoustic impedance changes, appropriate stability, a proper size that can enable extravasation of the vascular space, good compatibility, and the necessary safety protections for live tissues.

[a] *Research Center for Pharmaceutical Nanotechnology, Tabriz University of Medical Sciences, Tabriz, Iran. E-mail: aghanejaday@tbzmed.ac.ir; Tel: +98 41 33367914*
[b] *Department of Medical Physics and Biomedical Engineering, Tehran University of Medical Sciences, Tehran, Iran. E-mail: h-ghadiri@tums.ac.ir*
[c] *Research Center for Molecular and Cellular Imaging, Advanced Medical Technologies and Equipment Institute, Tehran University of Medical Sciences, Tehran, Iran*
[d] *Department of Anesthesiology, University at Buffalo, Jacobs School of Medicine and Biomedical Sciences, Buffalo, New York, USA*

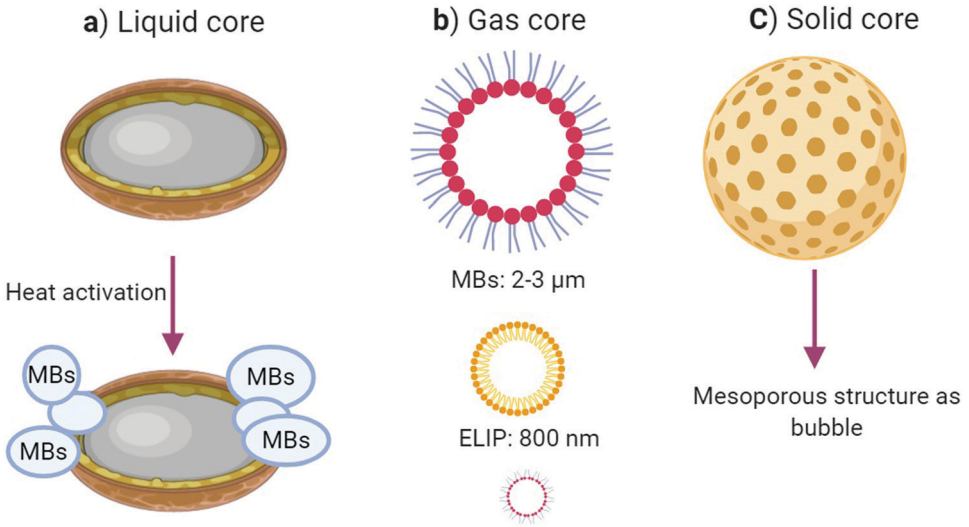

Fig. 1 Classification of USCAs based on core type.

Various parameters can affect the acoustic echo intensity of USCAs, including the particle size, core material, substances, and shell thickness.[11]

Although numerous NPs are utilized for many applications, including in diagnosis, targeted therapy, drug delivery,[12–14] we focus here on the use of diagnostic micro/nanomaterials as USCAs, which can allow cardiovascular and oncologic detection. Generally USCAs are divided into three classes based on the type of their cores; gas, solid, and liquid (Fig. 1). In the following, some properties of the most recent USCAs in these classes are summarized.

2. Ultrasound contrast agents (USCAs)

2.1. USCAs with a gas core

USCAs with a gas core induce high acoustic impedance differences within tissue interfaces, and they can generate the highest acoustic intensity among the other classes. The utilization of gas-core USCAs for the induction of ultrasound contrast started in 1980, in which microbubbles (MBs) were produced by agitating normal saline serum using two syringes connected to a three-way stopcock. The designed MBs enabled a rigorous acoustic intensity when employing an echocardiogram device from a cardiovascular system. USCAs in this field are divided into microbubble (MB) or nano-bubble (NB) groups based on their size. MBs are often stabilized by lipid, synthetic polymer, or protein coatings.[15]

Notwithstanding that the echo intensities of MBs are stronger than NBs, they suffer from poor stability in the bloodstream, a complex structure, and a shorter circulation lifetime due to their rapid detection and elimination by the reticular endothelial system (RES). Also, MB gas-core USCAs cannot be actively targeted for extravascular lesions because of their large sizes. These features have mainly restricted their applications to vascular space imaging, evaluating cardiac chambers, or targeting the intravascular markers of cancer.[16] Even so, some targeted MBs have entered the primary clinical phases; some of the latest successes are presented in the applications section briefly.

It is worth noting that there is in fact a strong correlation between the particle size and acoustic echo reflectivity. On the other hand, NB gas-core USCAs can escape from the RES, penetrate the tumor tissue through the endothelial gap, and accumulate at the target site. Several microbubble USCAs, *e.g.*, Definity, Echovist, and Sonovue, have been approved for clinical applications. USCAs with a gas core can be covered by lipid or polymer shells. These USCAs are either composed of gas or converted to gas by a unique reaction. They have some advantages like a high biocompatibility, favorable biodegradation, easy large-scale fabrication, simple surface modification, and satisfactory acoustic echogenicity.[17] This type of USCAs includes nano-bubbles (NBs), echogenic liposomes (ELIPs), gas vesicles (GVs), and gas-producing nanoparticles (GPNPs).

The structures of NBs consist of a gas core with a coating layer, including lipid, protein, polymers (*e.g.*, poly-lactic-*co*-glycolic acid (PLGA), poly-lactic acid (PLA), and polyethylene glycol (PEG)), to optimize the stability of the NBs' structure. Furthermore, several strategies, such as employing a heavy gas core and conjugation with a targeting agent, have been implemented to maximize the stability of NBs.[18,19] Due to their small size, they can be actively targeted in the extravascular space to detect cancer, though they have a relatively short half-life and lower stability. In one study, Yang *et al.* engineered nano-sized bubbles conjugated with affibody to detect human epidermal growth factor receptor 2 (HER2) overexpressing breast cancer cells using a conventional ultrasound scanner. The *in vitro* and *in vivo* images revealed that the NBs-affibody could be used as targeted USCAs in breast cancer diagnosis.[20] Also, several targeting moieties have been conjugated to NBs, including prostate-specific membrane antigen (PSMA), anti-vascular endothelial growth factor (VEGFR) antibodies, and ovarian cancer antigen (CA-125), to create novel targeted ultrasound contrast agents.[21–23]

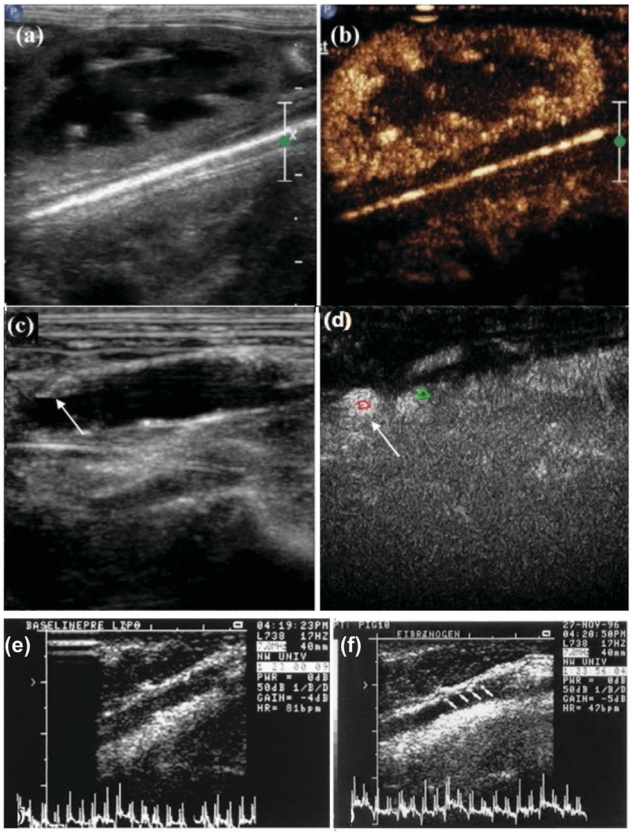

Fig. 2 Biotinylated nano-bubbles for the *in vivo* US imaging of rabbit kidney (a) without NB injection and (b) after the injection of anti-VEGFR-2-conjugated NBs. Visualization of the abdominal aorta (c) without NB injection and (d) after the injection of the targeted NBs. Adapted with permission from ref. 22. (e) Comparison of the intravascular ultrasound (IVUS) images of the left carotid of swine after an injection of saline and (f) after an injection of targeted ELIPs. Adapted with permission from ref. 25.

For example, anti-VEGFR-2 armed NBs were fabricated to selectively target the aorta atherosclerotic plaque in animal models (Fig. 2a–d).

ELIPs are nanoscaled sacs with polar lipid bilayer shells in which air is entrapped inside their core or between phospholipid bilayers. They are used to enhance the ultrasound signal intensity. Due to their small size, liposomes can escape the vessel space and accumulate inside the tumor tissue. Furthermore, they can even be actively targeted by special binding moieties to connect to the surface, which subsequently enhances the acoustic signal. As mentioned above, the core between the liposome walls is filled with gas. ELIPs, as ultrasound contrast agents, enhance the ultrasound image contrast more than that of solid cores while their induced contrast is less than that of MBs. For bubble entrapment within the liposome structure, special engineering is required to obtain a better echo intensity from the liposomes[24,25] (Fig. 2e and f).

Gas vesicles (GVs) are another type of novel gas-core ultrasound contrast agents. These vesicles are gas-filled protein shell enclosures with cylindrical shapes of a size in the range of 44–600 nm that have high gas permeability and are resistant to water penetration. These GVs may emanate from natural biological structures containing genetically encoded gas nanostructures formed by cyanobacterial and haloarchaeal host organisms or from *Escherichia coli* that can produce appropriate *in vitro* and *in vivo* acoustic echoes. These vesicles are often coated with gas vesicle protein A or B (GPA/B) or an external scaffold protein called gas vesicle protein C (VGC).[26–29]

GPNPs contain reactive compounds inside their base or shell, which release their compositions at temperatures higher than 42 °C. Following decomposition, they generate oxygen (O_2) or carbon dioxide (CO_2) gasses when reaching the target site. The released gas is used as an ultrasound contrast agent that enhances the acoustic intensity. Kang *et al.* developed a US contrast platform based on poly vanillin oxalate (PVO) NPs, which generate CO_2 through hydrogen peroxide (H_2O_2)-triggered bubbles. These theranostic NPs significantly increased the ultrasound echo intensity due to accumulation at the liver target site.[30] In another study, Min *et al.* offered a new strategy for CO_2-producing bubbles as theranostic ultrasound contrast agents entitled gas-NPs with high performance for tumor investigation. These contrast agents have a higher echo intensity that requires employing a high-frequency ultrasound scanner with novel gas-generating NPs both in *in vitro* and *in vivo* settings.[31] In another report, H_2O_2 was converted to oxygen (O_2) bubbles by decorating magnetic nanoparticles (MNPs) on black phosphor sheets, which increased the acoustic intensity during US imaging. This acoustic enhancement appeared to be due to the overexpression of these reactive radicals at the tumor site rather than the normal tissues in the presence of magnetic nanoparticles (MNPs) through an active or inactive targeting mechanism. As a reminder, the intensity and efficiency of gas production depend on the temperature, hydrogen peroxide concentration, and acidic environment.[32] Some of the most critical studies on USCAs containing a gas core are summarized in Table 1.

2.2. USCAs with a liquid core

Generally, in terms of echogenicity and stability, liquid-core USCAs have advantages over gas-core USCAs and disadvantages over solid-core USCAs. Liquid-core USCAs provide poor contrast enhancement because of their weak acoustic scattering inside the arteries due to their low impedance. In this regard, liquid-based materials, such as perfluorocarbon (PFC), including perfluoro-pentane (PFP), perfluorooctyl bromide (PFOB), and per-fluoro-hexane (PFH), if they accumulate in the target tissue/cells or change phase from liquid to a gas by applying thermal energy, either or both, have produced an impressive echo in preclinical experiments.[39]

Nanodroplets (NDs) as USCAs consist of a liquid core with a low boiling point, and include perfluorocarbon (PFC), perfluorooctyl bromide (PFOB), and perfluoro-pentane (PFP) encapsulated with an organic shell. These can be converted from a liquid phase to the gas phase upon heating. They are also called phase-change droplets (PCDs).[40]

The NDs can be transformed based on activation or a radiation source trigger through an ultrasound beam with a frequency-dependent heat generation pulse duration and variable temperature, which is the basis for acoustic droplet

Table 1 USCAs containing gas cores

Core type	Shell materials	Size (nm)	US mode	Freq. (MHZ)	Destructive threshold (MI)	Half-life *in vivo*	Lesion detection	Advantages/ disadvantages	Ref.
Biotin–DSPE	PEG_{2000} lipid	320	D Mode	NA	NA	NA	Atherosclerotic plaque-aorta	Long-term stability, targeting VEGFR2	22
DSPE–C_3F_8	$mPEG_{2000}$ lipid	277	CHI Mode	12	0.1	30 min	Prostate cancer	High stability, improved sensitivity and specificity for PSMA	33
C_3F_8	PEG-lipid	533	B & CE Mode	13–24	NA	10 min	Breast cancer	Long-term stability targeting AS1411	34
DPPE–DPPG	Lipid	1400	B Mode	20	NA	120 min	—	High stability, high echo, no toxicity	35
Raw bovin milk HEPES	BSA	110	B & CHI Mode	40	NA	—	Synovial fluid knee	No toxicity	36
$CaCO_3$	PDA–BSA–RBC	572	B Mode	40	NA	90 min	NA	High stability, high echo	37
$CaCO_3$	Polymer Pul-PCB	380	B-Mode	40	NA	60 min	Liver Hpg2	High stability	38
Bacteria–archaea	Protein	45–600	CHI Mode	5–20	NA	20 min	IVC liver	High stability and biocompatible	29

vaporization (ADV). Also, micron-sized bubbles could be obtained from near-infrared (NIR) irradiation, which is the basis for optical droplet vaporization (ODV). There are other stimulation strategies for converting the liquid phase to gas, including the use of magnets or magnetic, microwave, and radiofrequency droplet vaporization (magnetic droplet vaporization (MDV), microwave droplet vaporization (MWDV), and radiofrequency droplet vaporization (RFDV)). In the MDV method, the magnetic NPs can potentially generate heat under a magnetic field induction and release the encapsulated materials inside the NPs, subsequently increasing the ultrasound image contrast. Due to NIR's lower penetration, the RFDV stimulation amount is reduced compared to in ADV stimulation by the US beam. ADV has a higher penetration depth, and it is consequently more efficient in phase transformation.[41–43] Some of the USCAs containing solid cores are summarized in Table 2.

2.3. USCAs with a solid core

Solid-core USCAs have been developed as suitable surrogates to other USCAs for ultrasound contrast enhancement due to their unique properties. These properties include higher stability and desirable acoustic impedance changes between the solid-core materials and soft tissue. These features of solid-core USCAs lead to more robust reflectivity production, an improved signal to noise ratio (SNR), and more contrast enhancement. Solid-core USCAs have high echo intensities, both intravascular and within the soft tissues.[49,50]

These NPs have various features and select properties, including small size, multi-functionality, favorable stability, facile fabrication process, highly targeted turnover, high abundance, and versatile structures. Typically, solid-based ultrasound contrast agents have a relatively lower acoustic intensity than organic types, *e.g.*, MBs. Solid-core agents have bases made up of different materials, including silica, gold, carbon, magnetic, which are reviewed in the following.[51] Fig. 3 schematically illustrates the different types of solid NPs that are currently employed as USCAs.

Silica-based NPs have drawn significant attention as USCAs owing to their select properties, such as biocompatibility, unique porosity structure, large pore volume, high specific surface area, and controllable particle size, which has seen them proposed as enhanced USCAs with broad applications. Silica-based NPs are

Table 2 USCAs containing liquid cores

Core type	Shell material	Size (nm)	US mode	Freq (MHZ)	Phase transition	Destructive threshold (MI)	Half-life *in vivo*	Lesion detection	Advantages/disadvantage	Ref.
PFB	PEG_{5000}	114	B Mode	4	Liquid to gas (ADV)	1.7	45 min	Fibrosarcoma	High echo, minimal side effects	44
PFP	PEG-FA	47	B & CE Mode	5–12	Liquid to gas (ADV)	0.1	30 min	Prostate	PSMA targeting, long-term stability	33
PFH	RBC-IR780	261	B & CE Mode	NA	Liquid to gas (ADV)	—	—	—	High stability	45
PFP	PLGA-PVA	294	B & CE Mode	7.5	Liquid to gas (ODV)	NA	4 h	Tissue tumor	Dual modality (US-MRI), minimal side effects	46
PFH	PLGA-PVA	435	B Mode	30	Liquid to gas (ODV)	NA	2 h	Lymph nodes	High sensitivity/stability, low toxicity	47
DFB	PEG-GLC-CYN	400	B Mode	8	Liquid to gas (ODV)	1.2	NA	—	Multimodal, high stability	48

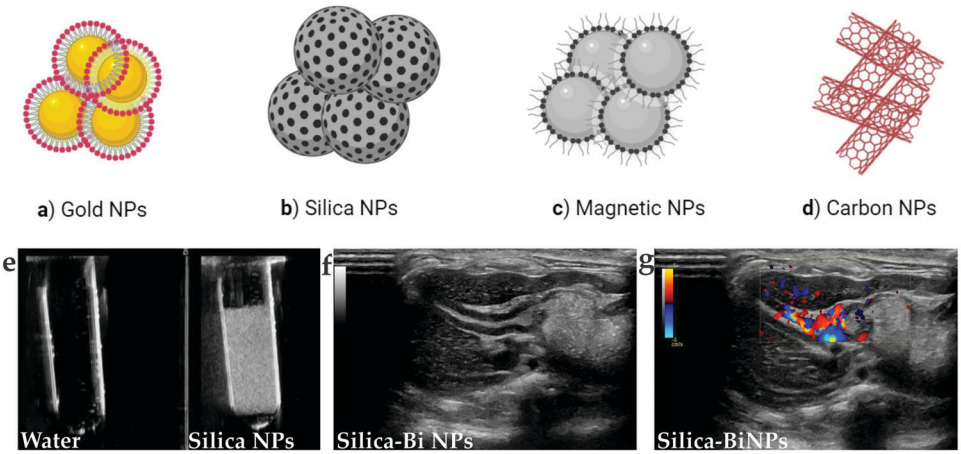

Fig. 3 Solid-based nanoparticles as USCAs in ultrasound imaging (a–d). (e) *In vitro* US images of mesoporous silica nanoparticles. *In vivo* US images acquired in mice after the injection of silica–bismuth NPs (f) under the B fundamental imaging modeand (g) under the Doppler imaging mode.

easy to surface modify, which allows them to be synthesized and designed in different ways and using different compositions, including solid silica, mesoporous silica nanospheres (MSNs), Stober silica nanospheres (SSNs), mesocellular foam (MCF), rattle-type, hollow mesoporous silica nanoparticles (HMSNs), exosome-like silica (ELS), and silica-based composites. A suitable echo can be achieved in the solid form due to this type's solid nature, which allows higher impedance differences. In HMSNs, a desirable echogenicity can be produced. Furthermore, with a unique rattle-type design, an increase in US echo over HMSNs has been observed.[52–54]

Carbon-based NPs in the form of multi-walled carbon nanotubes (MWCNTs) can effectively increase the US signal compared to clinical contrast media (SonoVue) and graphene oxide. This carbon design type has succeeded in extending the echo time to show internal organs, both *ex vivo* and *in vivo*, during US imaging. The excellent echo for such a design may be due to the entrapment of small bubbles in the nano complex walls, making a considerable impedance difference.[55]

Gold in certain forms and morphologies can have major diagnostic applications in US imaging, *e.g.*, in echogenic enhancers. For example, gold nanoshells (NSs) have excellent echo intensity in both B and pulse inversion harmonic ultrasound imaging. Also, the integration of gold with other materials, such as PFH and PFOB, with unique light absorption properties enables laser or high-intensity focused ultrasound (HIFU) conversion to heat and MB production, facilitating US contrast enhancement.[45,56]

Moreover, magnetic NPs can be excited by an external magnetic field. This process produces heat and then diffuses the produced heat to the surrounding environment. The operation mechanism in the presence of magnetic NPs inside a target site in which a gas is trapped is such that when the area is exposed to a magnetic field while performing simultaneous US imaging, due to the release of gas inside the magnetic NPs under heating, a suitable echo can be obtained.[57] Selected categories of USCAs containing solid cores are summarized in Table 3.

3. Ultrasound detection methods for the qualitative and quantitative assessment of contrast-enhanced images

Both targeted and non-targeted USCAs can be detected with various US imaging methods, including B-mode, Doppler (power

Table 3 USCAs containing solid cores

Core type	Shell materials	Size (nm)	US mode	Freq (MHZ)	Destructive threshold	Half-life *in vivo*	Lesion detection	Advantages/ disadvantages	Ref.
Silica	APTES-HER2	NA	B Mode	10	—	—	Breast	High stability, low toxicity, biocompatible	58
Silica	APTES-CYN	384	B & D Mode	5	1.3	60–120 min	Myocardium	Biocompatible, biodegradable	59
Gold	BSA-ICG	51	B Mode	33	—	—	—	High stability	60
Carbon	Protein	279	B & CE Mode	NA	—	20 min	Breast	Easy modification	54
Carbon	Silica	20–30	B & THI Mode	5–12.5	0.9	—	—	No toxicity	61
Iron	PEG-PLGA	9–18	CE	NA	—	72 h	Ovarian	Biocompatible, high stability, dual modal (US-MR)	62

or color), harmonic imaging, pulse inversion and multi-pulse imaging, and the contrast mode technique.[63]

Typically the B-mode and power or color Doppler imaging modalities are primary used in clinical practice. The B-mode is the most common US imaging method, which shows the organs in gray levels corresponding to the amplitude of the returned acoustic intensity. Still, the Doppler mode mainly demonstrates tissue perfusion, including allowing assessing stenosis or a lack of flow of large arteries up to 200 μm in diameter.[64] In harmonic imaging, also called non-linear scattering response, which employs a specific frequency (*e.g.*, 1F), the microbubbles contrasts will have non-linear contraction and expansion. In contrast, the surrounding tissues have regular oscillation, resulting in receiving waves 2F in frequency. The harmonic signal can be amplified and detected using a proper filtering technique (such as amplitude modulation and pulse inversion). It has been shown that harmonic imaging, contrast mode, and power Doppler imaging provide higher resolution, a stronger SNR, and greater details of blood flow, respectively.[65]

However, these modes may not detect specific conditions, including microcirculation within the vessels and tiny changes of the tissues in the early stages. Using USCAs, ultrasound sensitivity has improved its utility in diagnosing lesions, quantifying microvascular blood volumes, and assessing he blood flow to vital organs in humans.[66] In this regard, several techniques have been suggested; in the first method, there is no need for continuous US imaging, and obtaining an image of the target site at certain delayed phases is sufficient to prevent signal interference between the target tissue's circulatory system. Also, ideally USCAs will have a desirable opportunity to accumulate in the target tissue. The delay time depends on the contrast agents' core, shell, and target tissue structure. Contrary to the above-mentioned method, continuous US imaging of the target site should be performed by another approach. However, the curves' increase and decrease in signal intensity can be investigated. Ultimately, the images are subtracted from each other. There are several significant points in contrast-enhanced ultrasound (CEUS) imaging, and in particular, choosing the best imaging protocol is always an essential part of clinical imaging tasks, such as the optimal choice of using plane waves or focused imaging, the values of the focal depth, the F-number, mechanical index, dynamic range, bandwidth, and number of angles, which all play drastically important roles. Moreover, optimizing the structure of the transducer, selecting the appropriate detection mode, and choosing the proper qualitative and quantitative analysis methods are recommended. Furthermore, early and delayed phases should be evaluated in *in vivo* ultrasound experiments using targeted USCAs.[67]

Several models and methods have been developed for the quantitative analysis of US images to improve their diagnostic power. One of the most used quantification methods is the analysis of the time-intensity curve (TIC). TIC is the curve that shows changes in the echo amplitude over time and is extracted from the administered USCA route. It can be used to evaluate the wash-in and wash-out or increase and decrease in intensity over time due to the transfer of USCAs through the elective tissue. Generally, this method is known as temporal analysis. On the other hand, other parameters, such as the blood flow, contrast dose, area under the curve (AUC) for peak enhancement (PE), and volume, may be extracted by using this method.[67]

Furthermore, CEUS imaging for probing tissue perfusion, TIC, as well as statistics-based time-Nakagami curve (TNC) approaches can be used for tissue perfusion quantification. As the most recent development in this era, window-modulated compounding (WMC) Nakagami parameter ratio imaging has been used to overcome the inefficiencies of TNC in tissue clutters and in the presence of sub-resolvable effects.[68]

There is another quantitative analysis method named spatial analysis. In this analysis method, informative parameters, like the regional density uniformity and type of intravascular plaque lesions, are extracted from the perfusion and distribution of USCAs. The regional density uniformity can be used for detecting whether the cancer is malignant or not. It is worth mentioning that spatial analysis can be used with abnormal and very small vessels, in which temporal analyses are inefficient.[68] By integrating temporal and spatial analyses, another methodology known as spatiotemporal analysis can be seen. In this method, more comprehensive information, including on the vascular architecture, detailed perfusion, fractal dimensions, and nano contrast dispersion, is obtained from an arbitrary region of interest (ROI).[68]

Furthermore, in a latest attempt, due to the need to assess several parameters simultaneously, the multiparametric image analysis method using machine learning has been developed.[69] A significant development in the quantitative analysis of CEUS images has been obtained using radiomics methods to classify and evaluate some malignancies. Also, machine learning was applied in one study through a random forest classification algorithm, using the labels extracted from histopathology data from radical prostatectomy specimens as a reference to draw benign and malignant ROIs.[70]

4. Application trends of USCAs in the diagnosis of diseases

In recent years, with the improvement of USCAs, more information is available on pathological and physiological conditions. Therefore, the US modality has found broad applications in visualizing the body structure, including vessel evaluation and assessments of pathologic conditions. Several studies have focused on specific ultrasound contrast agents or a particular disease, and have illustrated the improvement of contrast-enhanced ultrasound imaging techniques for detecting particular cancer.[71,72]

4.1. USCAs in cardiovascular imaging

USCAs have been developed for both clinical and preclinical cardiovascular applications, with the major clinical applications

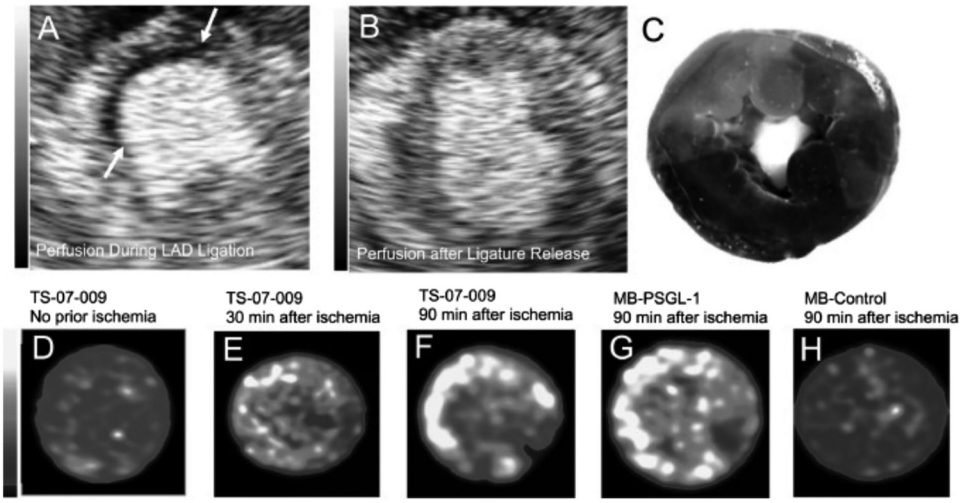

Fig. 4 US images of LAD ischemia in canine heart. Short axis myocardial perfusion images (A) during ligation of the LAD suture and (B) after release of the LAD suture (arrows indicate the location of the ischemic zone. (C) Phthalocyanine staining image of the perfused zones (dark) and ischemic regions (bright red). TS-07-009 accumulation images in (D) the baseline heart, (E) at 30 min and (F) 90 min post LAD ischemia cessation. (G) Uptake of P-selectin-conjugated MB (MB-PSGL-1) and (H) unarmed MBs (control group) 90 min post cessation of ischemia. Adapted with permission from ref. 78.

focused on the cardiovascular field using USCAs based on MBs. Applications have been established for the delineation of valvular, atrial, and ventricular cavities malfunctions, as well as for demonstration of endocardia boundaries in myocardial perfusion, and for the visualization of inflammation, thrombosis, and ischemic lesions. Some USCAs have been commercialized and used in the clinic, including development as a myocardial contrast to display tissue perfusion or for red blood cell (RBC) tracking. Injected MBs represent the volume of blood entering the myocardium through the microcirculation; thereby increasing the echo signal.[73–75]

Inflammation is a pathophysiological manifestation of vascular disease, in which leukocytes are activated and transported to the extravascular space and accumulated in inflamed tissues. Receptor mediators with integrin, P-selectin, and E-selectin integrated MBs are used to display myocardial inflammation, signs of ischemic lesion, or the presence of an atheroma plaque. Furthermore, endothelial inflammation occurs in the following conditions: atherosclerosis, ischemia, and implant rejection, which can be detected by antibody attached intercellular adhesion molecule-1 (ICAM1) and P-selectins conjugated with MBs.[76,77] Fig. 4 presents the ultrasound imaging of left anterior descending coronary artery (LAD) ischemia in a canine heart using TS-07-009 (MBs conjugated with MFG01035 recombinant protein) and P-selectin conjugated MBs (MB-PSGL-1). The results reveal that MB-PSGL-1, with more selectivity to P-selectin than E-selectin, exhibited a higher uptake at the ischemic sites than TS-07-009 with a similar selectivity to P- and E-selectin (Fig. 4F and G).[78]

Angiogenesis describes the formation of new capillaries from pre-existing vessels and is prone to bleeding into the atherosclerotic plaque, which can activate the platelets and cause thrombosis. Briefly, hypoxia occurs when an atheroma plaque grows up in the arterial wall, which is considered a triggering factor for the development of angiogenesis, also known as vasa-vasorum. Angiogenesis plays a vital role in assessing atheroma plaque progression deposited between the vascular walls; there is also a correlation between atherosclerosis and angiogenesis.[79]

In this regard, several markers activated on endothelial cells, including integrin ($\alpha_v\beta_3$) and vascular endothelial growth factor (VEGFR-2) conjugated with MBs as contrast-enhanced ultrasound agents, have been developed. It has been shown that the mean pixel intensity (MPI) of VEFR-2@ MBs as CEUS is higher than targeted $\alpha_v\beta_3$ in the detection of angiogenesis.[80]

The targeted ultrasound imaging of atherosclerosis has two specific features compared to other endothelial lesions: first, the loss of signal demonstration in the atheroma plaque regions and second, the inability to identify atherosclerosis using a low-frequency system (contrary to other lesions) in inflammation and angiogenesis (in which this lesion requires high-frequency devices, such as catheter-based intravascular ultrasound (IVUS)).[81] Several studies have explored atherosclerotic lesions, mostly with a focus on determining the activated platelets and evaluating inflammation for the early detection of plaque progression; therefore, they utilize the glycoproteins on platelets bonded MBs to monitor plaque progression or for an assessment of the response to treatment intervention.[82,83] Conversely, other studies have applied inflammatory markers, such as vascular cell adhesion molecule-1 (VCAM1) and ICAM1, to identify the atheroma plaque situation.[84]

In one study, magnetic nanoparticle microswarms (MNP micSW) were used for the real-time investigation of swarm formation in blood vessels under ultrasound Doppler imaging. As shown in Fig. 4, the rotating micSW disrupted the normal flow of blood cells. Moreover, US waves emitted to micSW, providing an ultrasound Doppler imaging modality for medical imaging-guided SW navigation in the blood vascular system (Fig. 5).[85]

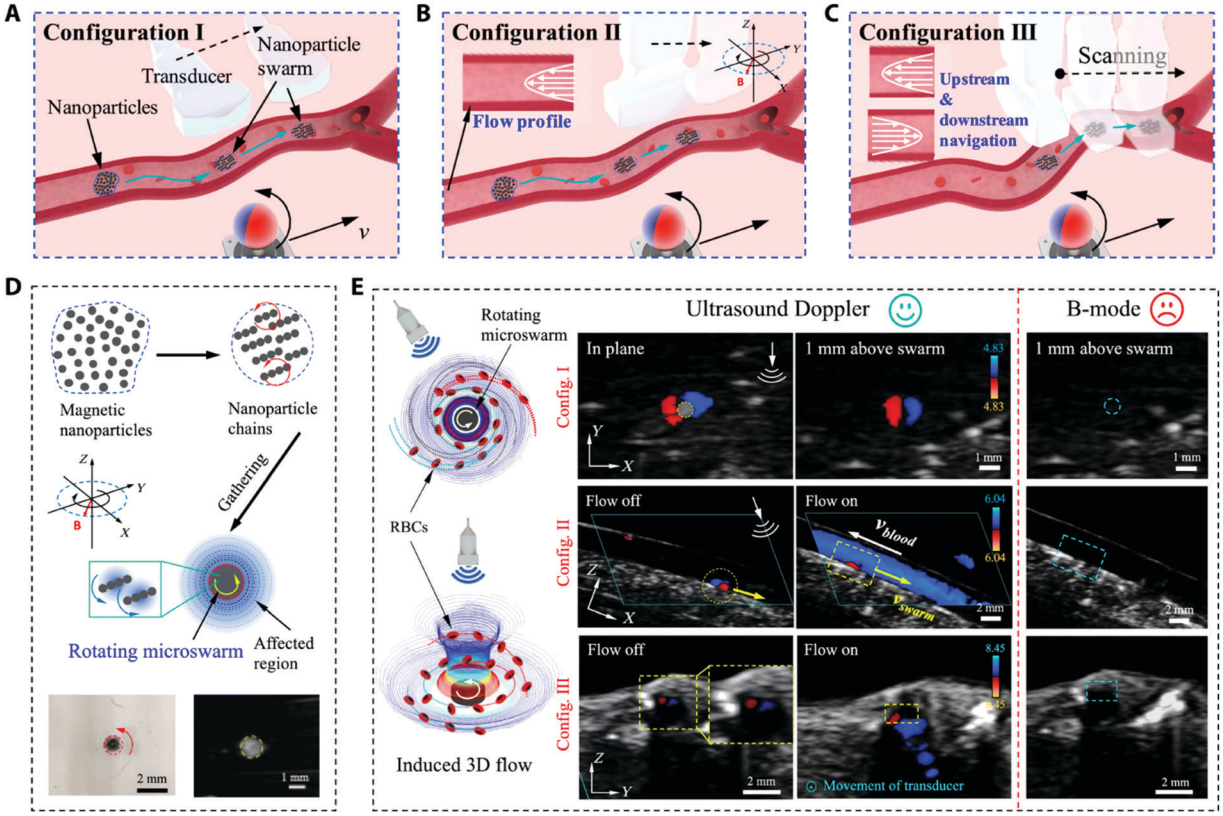

Fig. 5 (A–C) Schematic of the US Doppler image-guided swarm (SW) formation and motion in blood vessels. (D) SW formation process, and the magnetic and hydrodynamic interactions of the rotating NPs chains that cause the assembly of the nanoparticles to be a rotating microswarm (micSW). Left (light microscope image) and right panels (B-mode US image) illustrating a micSW in water–glycerol solution and porcine whole blood, respectively. (E) The US Doppler signal around a rotating micSW in blood. Blue dashed lines signify the theoretical position of the micSW in the B-mode US images (right column). Adapted from ref. 85.

In clinical practice, Doppler ultrasound and echocardiography have been used to demonstrate extensive or moderate deep venous thrombosis (DVT) and intracardiac clots, respectively; however, these techniques cannot display the microvascular clots, especially in carotid and coronary arteries. On the other hand, it is essential to distinguish acute thrombosis from chronic thrombosis for providing proper treatment promptly. The use of a targeted contrast agent in ultrasound is recommended, such as for thrombosis using thrombin-responsive NBs.[86] The application of USCAs in cardiovascular imaging is summarized in Table 4.

4.2. USCAs in cancer imaging

Ultrasound contrast agents as markers of vascularity and microcirculation for the early recognition of oncologic cases have been developed rapidly, typically employing different targeted ligands. In this context, angiogenesis is an essential process in demonstrating the severity of the invasion and metastasis of tumors and for delineating the extent of tissue adaptation to chronic ischemia. As mentioned in the previous section, the following target moieties markers are used to detect angiogenesis: VEGFR, $\alpha_v\beta_7$ integrin, monoclonal antibody, and arginine–glycine–aspartic acid (RGD). The most targeted uses of USCAs are related to breast, colon, prostate, and ovarian cancers, respectively (Table 5). Accordingly, based on the type of ligand with a specific application, they are divided into a number of separate categories representing the oncologic applications, as discussed below.

4.2.1. Urogenital system cancers. The most common malignancies in the urogenital system consist of kidney, bladder, prostate, and testicular tumors, which can be detected by ultrasound imaging. Since the types of urogenital cancers are different, the targeting ultrasound contrast agents used for their detection are different; therefore, the description of the diagnosis using CEUS is given separately. There are limited studies on renal tumor detection by targeted ultrasound contrast agents. However, in one study conducted by Rojas and coworkers, the response of the renal cell carcinoma (RCC) rate to therapeutic strategies was assessed using VEGFR-1 targeted MBs, which could detect disease progression in the early stage.[100]

Prostate cancer is the fourth most common cancer in men. The diagnosis of this cancer in the first stage can reduce the mortality rate. In early attempts, researchers focused on evaluating prostate malignancy's angiogenesis employing targeted MBs that express VEGFR2, ICAM1, and $\alpha_v\beta_3$-integrin. In the next step, a new ligand PMSA aptamer was conjugated with NBs in a mice model, which reduced previous studies' limitations

Table 4 USCAs in cardiovascular imaging

Lesion type	Types of USCAs	Size of USCAs	Targeting moieties	Lesion site	Ref.
Inflammation	MBs	2.2 μm	P-selectin	Abdominal aorta	87
		3.4 μm	E-selectin	Myocardium	88
		<8 μm	P&E selectin	Myocardium	78
		1.5 μm	VCAM1	Aorta	89
		1 μm	$\alpha_v\beta_3$	Carotid arteries	90
Atherosclerosis	MBs	<400 nm	ICAM1-VEGFR	Aorta	91
		NA	VCAM1	Thoracic aorta	92
		10 μm	Glycoprotein	Carotid Arteries	93
	NBs	200 nm	VEGFR2	Abdominal aorta	22
Myocardial ischemia	MBs	3.4 μm	E-selectin	Myocardium	88
		<8 μm	Dual(P&E) selectin	Myocardium	78
	HMSN	372.6 nm	—	Myocardium	59
Angiogenesis	MBs	2.8 μm	VEGFR2	—	94
		NA	$\alpha_v\beta_3$	Carotid	95
Thrombosis	MBs	1.6 μm	Thrombin	—	96
		NA	E-selectin	Iliac vein	97
	PFP	256.6 nm	Fibrin	Inferior vena cava	98

Table 5 USCAs in cancer lesions imaging

Body system	Organ	Types of USCAs	Targeting moieties	Size	Ref.
Urogenital cancers	Renal	MBs	VEGFR2	—	99
			VEGFR-FSHR	—	100
	Prostate	NBs	PSMA	533 nm	34
			RGD	210 nm	101
			ICAM1	683 nm	102
			CDCP1	172 nm	103
		Carbon	PSCA	75 nm	104
		PEG- PLA	—	2.5 μm	105
		MSN	—	161 nm	106
Gynecological cancers	Breast	MBs	B7-H3	1–4 μm	107 and 108
			iRGD-$\alpha_v\beta_3$	1–4 μm	109
		Gold-PLGA MBs	VEGFR2-P53	277 nm	110
		PFP-based NBs	—	362 nm	111
		PLGA-PEG NBs	mAb_{CAIX}	—	112
			AnnexinV	635 nm	113
		NBs	Aptamer AS1411	533 nm	34
		NB-Affibody	HER2	478 nm	20
		Au	Poly Dopamine	27.5 nm	114
	Ovarian	NBs	Pro GRP	378 nm	115
			CA-125	75 nm	116
		Pt(IV)/PLGA-PEG	cRGD	43 nm	117
		PLGA-SA/PFP	SA	383 nm	118
		NBs	VEGFR2	—	119
		Au	Peptide-Gly3	230 nm	120
	Cervix	MBs	anti-PD-L1 ab	939 nm	121
Respiratory cancers	Larynx	MBs	RGD	2.3 μm	122
	Lung	NBs	Liposome	378 nm	115
Gastrointestinal cancers	Bowel	MBs	P&E selectin	1–3 μm	123
		MBs	VEGFR2	—	124
		PFC-PDA	—	255 nm	125
	Liver	BR55	VEGFR2	1–4 μm	126
		MBs	VEGFR2	1–4 μm	127
		Nanogels	—	—	128
	Pancreas	MBs	VEGFR2	1.6 μm	129
			VEGF	—	130
			Thy1	1–3 μm	131

and increased the ultrasound imaging specificity. In the clinical phase, a group of researchers used BR55 (KBR integrated with MBs to provide an appropriate assessment of prostate cancer's malignant stages by targeted ultrasound imaging.[132] In another study, PSMA-targeted-NBs were developed as a biomarker of PSMA-negative PC3flu and PSMA-positive PC3pip for simultaneously imaging in a mouse model (Fig. 6). The results proved the active targeting and tumor accumulation by the PSMA-targeted-NBs.[21]

4.2.2. Gynecological cancers. Gynecological cancers referred to malignancies of women's reproductive organs, including ovarian, uterine, cervical–vaginal associated breast organs,

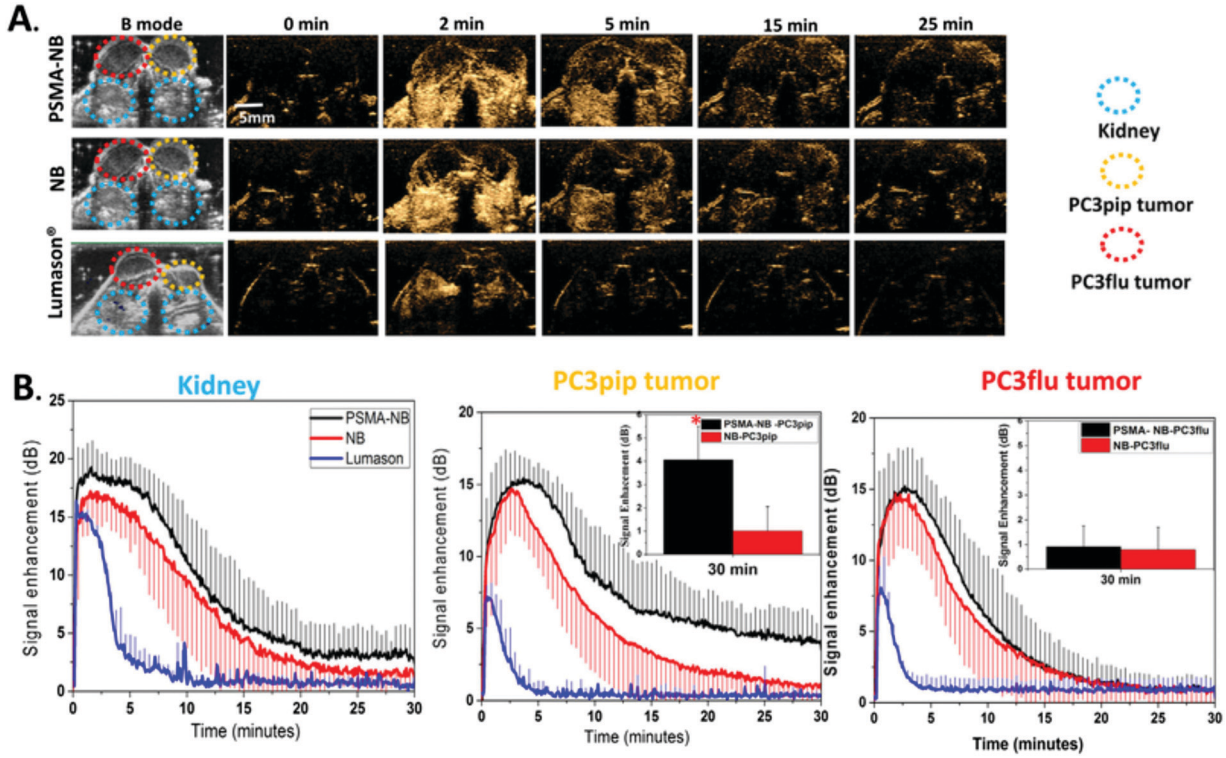

Fig. 6 (A) Comparison of ultrasound images of prostate cancer and kidney between PSMA-NB, NB, and Lumason USCAs in consecutive times. (B) Quantitative analysis in terms of the time–intensity curve (TIC) using USCAs in the kidney (left) and for two types of prostate cancer (middle and right). Adapted with permission from ref. 133.

which involve pathological conditions. Contrast-enhanced ultrasound imaging is one of the important modalities dedicated to the early diagnosis of gynecological cancers. Breast cancer is the most common cancer in women, mostly in women over 40 years old.[134] Much literature exists on several types of research into detecting breast lesion using various targeted ultrasound contrast agents; examples of these targeted ultrasound contrast agents for breast cancer applications both *in vitro* and *in vivo* include integrin ($\alpha_v\beta_7$) integrated iRGD-peptide targeted MBs, VEFR2 incorporated to MBs, Netrin bonded to MBs as single targeted USCAs and VEGFR2, HER2@PLGA conjugated with NB as dual-targeted USCAs and CD-276 (B7-H3) targeted MBs (Table 5). Contrast-enhanced MBs conjugated with kinase insert domain receptor (KDR), known as BR55, is expressed as VEGFR2. Even the clinical application of this contrast agent in breast cancer detection has been reported in humans, indicating that the increase in signal ultrasound corresponds to an overexpression in immunohistochemistry.[135]

Since ovarian cancer may have no symptoms, it is hard to diagnose this type of cancer in the early stages. However, it remains the most lethal of all gynecological cancers. In the evaluation of ovarian carcinoma, several targeted USCAs, including CA-125 targeted NBs ($\alpha_v\beta_3$) integrated Sonazoid (MBs-based), have been developed, which accumulate in the ovarian tumor and increase the ultrasound signal intensity significantly. In the human phase, BR55 targeting KDR has also been considered to detect ovarian cancer.[136]

In one study, MUC16 conjugated bismuth-coated mesoporous silica NPs (MSBi@MUC16-NPs) were used as dual modal US/CT contrast agents for the targeted diagnosis of cervical cancer in an animal model (Fig. 7). The results revealed that by employing MSBi@MUC16-NPs, the ultrasound echo intensity was enhanced for the targeted NPs, both at the cellular level and in a HeLa tumor-bearing animal model.[137]

4.2.3. Respiratory cancers/lesions. The applications of ultrasound for respiratory lesions in specific anatomical structures (existence of gas and bone in the respiratory system, whereby most of the transmitted echoes cannot pass and penetrate through the organs and almost of the signal is thus returned) compared to in abdominal-pelvis organs are usually limited to the diagnosis of childhood pulmonary disease and chest wall soft tissue lesions.[138,139] Wang *et al.* investigated small cell cancer lung (H446 cell lines) in a nude mouse model bearing a small cell lung cancer (SCLC) tumor by using NBs-encapsulated liposomes loaded with anti-pro-gastrin releasing peptide targeted ultrasound contrast agents, which demonstrated a significant increase in half-life circulation and ultrasound intensity compared with non-targeted NBs[115] (Fig. 8).

4.2.4. Gastrointestinal cancers. These malignancies refer to cancer of the alimentary path, including the esophagus, stomach, small and large bowel, and accessory organs, such as the liver, gallbladder, and pancreas. Using KDR-conjugated MBs can delineate minute lesions, such as tiny polyps, diverticula, intestinal perfusion, regional ischemia, and inflammation.

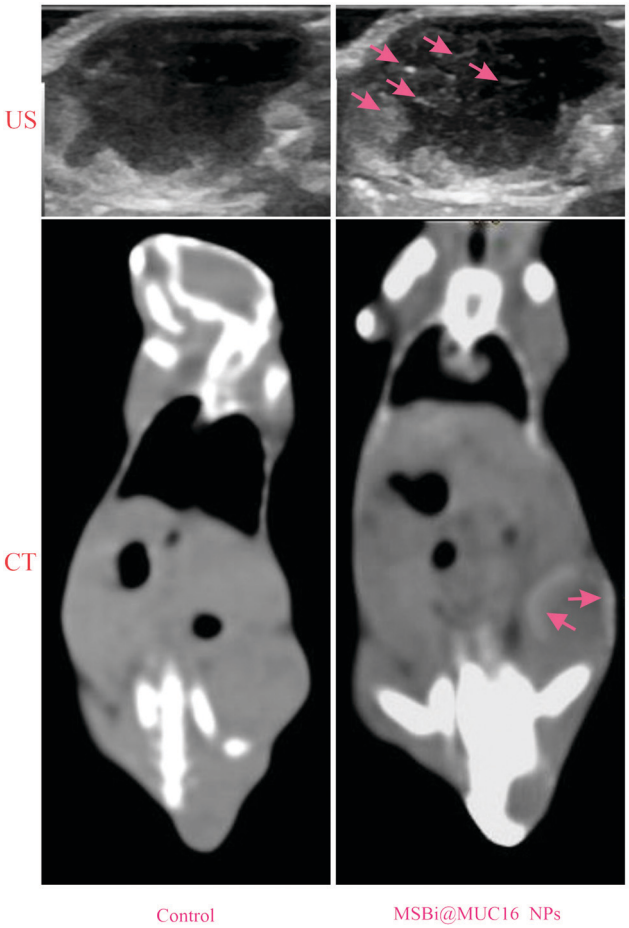

Fig. 7 US/CT targeted images of MSBi@MUC16 NPs in HeLa tumor-bearing BALB/c mice pre and post-injection of contrast agents. The contrast enhancement of the tumor site is apparent due to a high uptake of the targeted NPs. Adapted from ref. 137.

In multiple conditions, such as colitis, intestinal bowel diseases (IBD), and complications after radiotherapy, endothelial markers are overexpressed, such as P&L&E selectin and ICAM1. Several studies have recently been conducted to investigate the rate of angiogenesis and tumor perfusion as a sign of the response to treatment using MBs, targeting VEGFR2 by B and three-dimensional (3D) ultrasound mode imaging.[140] Several studies evaluated different tumors, such as hepatoblastoma and hepatocellular carcinoma, and it was found that in the case of hepatoblastoma, it is essential to consider cancer-related angiogenesis using a targeted contrast agent. In this context, Wu *et al.* were able to represent the enhanced echo intensity by using endoglin integrated MBs associated with angiogenesis.[141] Sorafenib as a protein kinase inhibitor is used for the treatment of hepatocellular carcinoma and renal cell carcinoma. As mentioned recently, to assess the response rate treatment related to hepatocellular radiotherapy in this era, Baron *et al.* demonstrated the successful early response to sorafenib as a chemotherapy drug to treat hepatocellular cancer in a mouse model by decreasing the ultrasound signal echogenicity.[142–144] For example, the UTMD treatment of liver tumors using VEGFR2-conjugated MBs in animal models revalued a strip blood flow signal for the intrahepatic tumor site.

Also, the CEUS of a tumor before UTMD indicated that the echo of the tumor site was enhanced after the injection of targeted MBs (Fig. 9).

One of the most common pancreatic cancers is ductal adenocarcinoma; and though it does not have a good prognosis, its detection and accurate staging can improve the patient's condition. In clinical practice, ultrasound imaging, the initial technique in substantial clinical applications, enabled pancreatitis detection, and allowed displaying the lesions and appearance staging of the adenocarcinoma. Ultrasound of the pancreas can be performed in various ways, including transabdominal, endoscopic ultrasound, intraoperative ultrasound (IOUS), and contrast-enhanced ultrasound (CEUS). Even by using targeted MBs conjugated with different ligands, intraoperative ultrasound can facilitate the differential diagnosis of pancreatic malignancy and tiny lesions of tumors. To achieve this goal, for displaying angiogenesis of a tumor and visualization of the neo-vasculature, several ligands

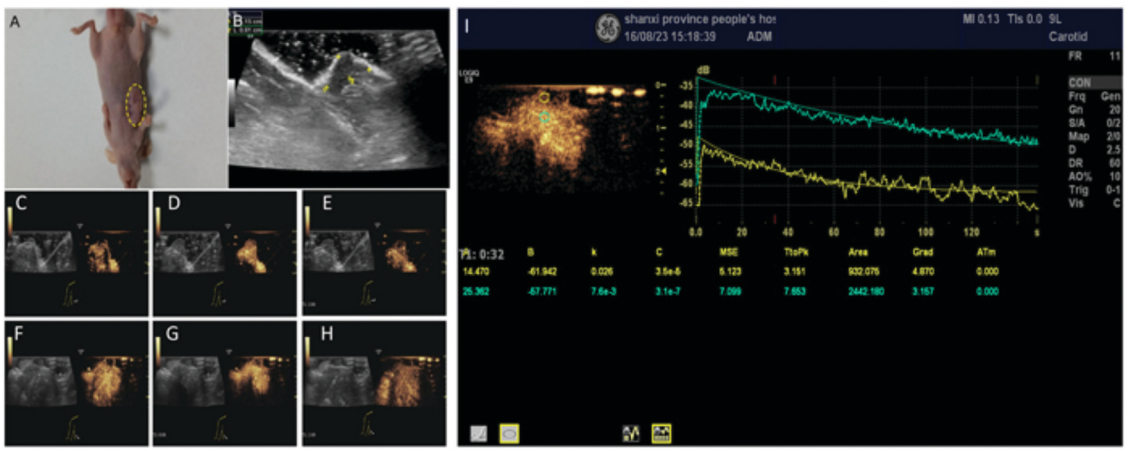

Fig. 8 (A) The tumor size was 1.18 ± 0.12 cm. (B–H) Quantitative analysis of the SCLC xenograft tumor in the early and late stage using targeted USCAs. (I) TIC related to normal and cancerous tissues. Adapted from ref. 115.

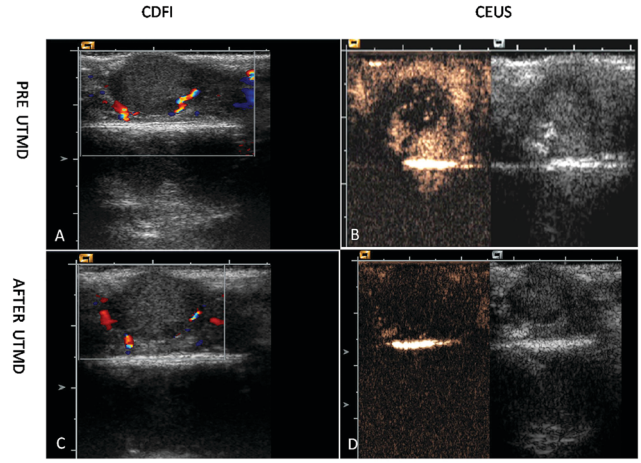

Fig. 9 CDFI and CEUS images of intrahepatic tumors in mice after 7 days of injection. (A and C) CDFI of the tumors before and after UTMD treatment. There was a strip blood flow signal around the tumor site when using CDFI. CEUS of tumor (B) before UTMD and (D) after UTMD (MBs in the tumor disappeared). Adapted with permission from ref. 141.

(VEGFR-2, integrin, endoglin, and Thy-1) integrating MBs have been tested in mice models or clinical trials.[112]

5. Challenges and future outlook

There are still some fundamental challenges to designing ideal USCAs. One controversial debate for utilizing USCAs is in designing and controlling the USCAs' size in the preparation steps. When contrast agents enter the body, circulate through the vascular and are distributed, they can interact with plasma proteins, which can lead to a change in the surface charge of the agents and also to their small size, giving rise to larger sizes. In such a way, regardless of the basis of USCAs, whether gas, liquid, or solid based, they are mainly eliminated by the reticulo-endothelial system (RES). Even if they succeed in avoiding clearance by the RES system, they cannot escape the vascular space. This phenomenon will be more significant if the ultrasound contrast materials are gas based or gas convertible materials with a larger size. In this situation, their circulation appears faster and they cannot extravagate into the tumor site, and consequently, their ability to target tumors is reduced significantly. As a reminder, some of the microbubbles are destroyed over time by the high ultrasound acoustic pressure.

In contrast, small-sized materials have a weak signal echo intensity, and are almost entirely removed by glomerular filtration by the kidneys. Hence, it can be said that the both clearance and distribution of USCAs are mainly determined by their size, and ultimately both approaches (large and small sizes) have confined limits in their detection capabilities. Therefore, a balance must be struck between the signal intensity and their size. It is expected in the near future, that some effort will be focused on synthesizing nano-sized drug-delivery systems engineered using gas-based USCAs to preserve the appropriate signal echo intensity.

With respect to the USCAs' size, solid-based ultrasound contrast agents tend to be ductile materials with favorable degradability and greater resistance to acoustic output compared to bubbles, which were the focus of the earliest attempts to provide novel synthesis methods with a simplified design of non-gaseous materials as ultrasound contrast agents, *i.e.*, as an alternative approach to gas-based USCAs. In this regard, the most current research approach is the development of solid-based USCAs by targeting different ligands to assist in reducing the amount of contrast agents to be applied. In this manner, researchers aim to pave the way toward the development of theranostatic materials to facilitate the drug-delivery process and to provide more effective treatment through ultrasound-guided imaging. The optimization of the imaging platform is required to increase the spatial resolution and enhance CNR, followed by the development of further desirable therapeutic strategies. With advances in technology in the fabrication and design of transducers, novel image processing techniques, and a fundamental change in pulse sequences, it is highly expected that cardiovascular diseases and oncologic conditions will be evaluated more accurately by ultrasound imaging and early-stage disease detection will be achieved.

Conflicts of interest

There are no conflicts to declare.

Acknowledgements

This work was supported by the Research Center for Pharmaceutical Nanotechnology, Tabriz University of Medical Sciences, Tabriz, Iran, and Department of Medical Physics and Biomedical Engineering, Tehran University of Medical Sciences, Tehran, Iran (grant number: 43096-30-02-98).

References

1 P. Lancellotti, M.-L. Nguyen Trung, C. Oury and M. Moonen, *Eur. Heart J.*, 2021, **42**, 110–112.
2 A. Tarighatnia, G. Johal, A. Aghanejad, H. Ghadiri and N. Nader, *Front. Biomed. Technol.*, 2021, **8**(3), 226–235.
3 A. Tarighatnia, M. R. Fouladi, M. R. Tohidkia, G. Johal, N. D. Nader, A. Aghanejad and H. Ghadiri, *J. Drug Delivery Sci. Technol.*, 2021, **66**, 102895.
4 N. Lassau, *Molecular Imaging in Oncology*, Springer, 2020, pp. 765–771.
5 N. Vahidfar, A. Aghanejad, H. Ahmadzadehfar, S. Farzanehfar and E. Eppard, *Int. J. Mol. Sci.*, 2021, **22**(9), 4597.
6 A. Aghanejad, A. R. Jalilian, S. Maus, H. Yousefnia, P. Geramifar and D. Beiki, *Iran. J. Nucl. Med.*, 2016, **24**(1), 29–36.
7 K. Rajamanickam, *Arch. Intern. Med. Res.*, 2020, **3**, 032–043.
8 C. Lau, P. Hess, T. Shreves and M.-S. Lee, *J. Diagn. Med. Sonograph.*, 2020, **36**, 479–487.

9 E. Di Naro, L. Raio, A. Basso and M. R. Catalano, *Pick Up and Oocyte Management*, Springer, 2020, pp. 49–72.
10 S. Siemer, D. Wünsch, A. Khamis, Q. Lu, A. Scherberich, M. Filippi, M. P. Krafft, J. Hagemann, C. Weiss and G.-B. Ding, *Nanomaterials*, 2020, **10**, 383.
11 J. Baier, A. Rix and F. Kiessling, *Molecular Imaging in Oncology*, Springer, 2020, pp. 509–531.
12 A. Aghanejad, A. R. Jalilian, Y. Fazaeli, D. Beiki, B. Fateh and A. Khalaj, *J. Radioanal. Nucl. Chem.*, 2014, **299**(3), 1635–1644.
13 P. N. Nabi, N. Vahidfar, M. R. Tohidkia, A. A. Hamidi, Y. Omidi and A. Aghanejad, *Int. J. Biol. Macromol.*, 2021, **174**, 185–197.
14 J. Kadkhoda, M. Akrami-Hasan-Kohal, M. R. Tohidkia, S. Khaledi, S. Davaran and A. Aghanejad, *Int. J. Biol. Macromol.*, 2021, **185**, 664–678.
15 A. L. Klibanov, *Invest. Radiol.*, 2021, **56**, 50–61.
16 M. Salih, S. M. Ali, N. Jena and K. Ananthasubramaniam, *Fut. Cardiol.*, 2020, **17**, 197–214.
17 A. Kosareva, L. Abou-Elkacem, S. Chowdhury, J. R. Lindner and B. A. Kaufmann, *Ultrasound Med. Biol.*, 2020, **46**(3), 479–497.
18 X. Gao, D. Guo, X. Mao, X. Shan, X. He and C. Yu, *Nanoscale*, 2021, **13**, 5333–5343.
19 M. L. Johansen, R. Perera, E. Abenojar, X. Wang, J. Vincent, A. A. Exner and S. M. Brady-Kalnay, *Int. J. Mol. Sci.*, 2021, **22**(4), 1983.
20 H. Yang, W. Cai, L. Xu, X. Lv, Y. Qiao, P. Li, H. Wu, Y. Yang, L. Zhang and Y. Duan, *Biomaterials*, 2015, **37**, 279–288.
21 R. H. Perera, A. de Leon, X. Wang, Y. Wang, G. Ramamurthy, P. Peiris, E. Abenojar, J. P. Basilion and A. A. Exner, *Nanomedicine*, 2020, **28**, 102213.
22 X. Zhang, M. Wu, Y. Zhang, J. Zhang, J. Su and C. Yang, *Colloids Surf., B*, 2020, **189**, 110861.
23 S. Nimmagadda and M.-F. Penet, *Front. Oncol.*, 2020, **9**, 1537.
24 D. V. B. Batchelor, F. J. Armistead, N. Ingram, S. A. Peyman, J. R. McLaughlan, P. L. Coletta and S. D. Evans, *Curr. Opin. Colloid Interface Sci.*, 2021, **54**, 101456.
25 S. M. Demos, H. Alkan-Onyuksel, B. J. Kane, K. Ramani, A. Nagaraj, R. Greene, M. Klegerman and D. D. McPherson, *J. Am. Coll. Cardiol.*, 1999, **33**, 867–875.
26 R. Wang, L. Wang, Y. Chen, Y. Xie, M. He, Y. Zhu, Z. Han, L. Xu, D. Chen and L. Zhang, *Curr. Med. Chem.*, 2022, **29**(8), 1316–1330.
27 A. Farhadi, G. Ho, M. Kunth, B. Ling, A. Lakshmanan, G. J. Lu, R. W. Bourdeau, L. Schröder and M. G. Shapiro, *AIChE J.*, 2018, **64**, 2927–2933.
28 A. Lakshmanan, G. J. Lu, A. Farhadi, S. P. Nety, M. Kunth, A. Lee-Gosselin, D. Maresca, R. W. Bourdeau, M. Yin and J. Yan, *Nat. Protoc.*, 2017, **12**, 2050–2080.
29 M. G. Shapiro, P. W. Goodwill, A. Neogy, M. Yin, F. S. Foster, D. V. Schaffer and S. M. Conolly, *Nat. Nanotechnol.*, 2014, **9**, 311–316.
30 C. Kang, W. Cho, M. Park, J. Kim, S. Park, D. Shin, C. Song and D. Lee, *Biomaterials*, 2016, **85**, 195–203.
31 H. S. Min, S. Son, D. G. You, T. W. Lee, J. Lee, S. Lee, J. Y. Yhee, J. Lee, M. H. Han and J. H. Park, *Biomaterials*, 2016, **108**, 57–70.
32 Y. Zhu, Y. Liu, Z. Xie, T. He, L. Su, F. Guo, G. Arkin, X. Lai, J. Xu and H. Zhang, *Nanophotonics*, 2021, **10**(12), 3339–3358.
33 R. H. Perera, X. Wang, Y. Wang, G. Ramamurthy, P. Peiris, E. Abenojar, J. P. Basilion and A. A. Exner, *Nanomedicine*, 2020, 102213.
34 K. Fang, L. Wang, H. Huang, M. Lan, D. Shen, S. Dong and Y. Guo, *Pharm. Res.*, 2020, **37**, 1–13.
35 K. D. Buchanan, S. Huang, H. Kim, R. C. MacDonald and D. D. McPherson, *J. Pharm. Sci.*, 2008, **97**, 2242–2249.
36 J. Osborn, J. E. Pullan, J. Froberg, J. Shreffler, K. N. Gange, T. Molden, Y. Choi, A. Brooks, S. Mallik and K. Sarkar, *Nanoscale Adv.*, 2020, **2**, 3411–3422.
37 M. L. P. Vidallon, A. M. Douek, A. Quek, H. McLiesh, J. Kaslin, R. F. Tabor, A. I. Bishop and B. M. Teo, *Part. Part. Syst. Charact.*, 2020, **37**, 1900471.
38 S. Niu, G. R. Williams, J. Wu, J. Wu, X. Zhang, X. Chen, S. Li, J. Jiao and L. M. Zhu, *J. Nanobiotechnol.*, 2019, **17**, 95.
39 R. Guo, N. Xu, Y. Liu, G. Ling, J. Yu and P. Zhang, *Ultrasound Med. Biol.*, 2021, **47**(8), 2064–2079.
40 F. Eklund, M. Alheshibri and J. Swenson, *Curr. Opin. Colloid Interface Sci.*, 2021, **53**, 101427.
41 D. Qin, Q. Zou, S. Lei, W. Wang and Z. Li, *Ultrason. Sonochem.*, 2021, 105608.
42 D. A. Fernandes, S. Appak-Baskoy, E. Berndl and M. C. Kolios, *RSC Adv.*, 2021, **11**, 4906–4920.
43 Y.-S. Chen, Y. Zhao, C. Beinat, A. Zlitni, E.-C. Hsu, D.-H. Chen, F. Achterberg, H. Wang, T. Stoyanova, J. Dionne and S. S. Gambhir, *Nat. Nanotechnol.*, 2021, **16**, 717–724.
44 B. L. Helfield, K. Yoo, J. Liu, R. Williams, P. S. Sheeran, D. E. Goertz and P. N. Burns, *Ultrasound Med. Biol.*, 2020, **46**, 2861–2870.
45 Y. Liang, H. Yang, Q. Li, P. Zhao, H. Li, Y. Zhang, W. Cai, X. Ma and Y. Duan, *Cancer Chemother. Pharmacol.*, 2020, 1–14.
46 Y. Xu, C. Niu, S. An, S. Tang, P. Xiao, Q. Peng and L. Wang, *RSC Adv.*, 2017, **7**, 40791–40802.
47 L. Yang, J. Cheng, Y. Chen, S. Yu, F. Liu, Y. Sun, Y. Chen and H. Ran, *Sci. Rep.*, 2017, **7**, 45213.
48 S. Lin, A. Shah, J. Hernández-Gil, A. Stanziola, B. I. Harriss, T. O. Matsunaga, N. Long, J. Bamber and M.-X. Tang, *Photoacoustics*, 2017, **6**, 26–36.
49 N. S. Awad, V. Paul, N. M. AlSawaftah, G. ter Haar, T. M. Allen, W. G. Pitt and G. A. Husseini, *ACS Pharmacol. Transl. Sci.*, 2021, **4**, 589–612.
50 K. Ovejero Paredes, D. Díaz-García, V. García-Almodóvar, L. Lozano Chamizo, M. Marciello, M. Díaz-Sánchez, S. Prashar, S. Gómez-Ruiz and M. Filice, *Cancers*, 2020, **12**, 187.
51 P. Frinking, T. Segers, Y. Luan and F. Tranquart, *Ultrasound Med. Biol.*, 2020, **46**, 892–908.
52 A. Baeza and M. Vallet-Regí, *Pharmaceutics*, 2020, **12**(10), 957.

53 M. Du, Y. Chen, J. Tu, C. Liufu, J. Yu, Z. Yuan, X. Gong and Z. Chen, *ACS Biomater. Sci. Eng.*, 2020, **6**, 2904–2912.
54 L.-Q. Zhou, P. Li, X.-W. Cui and C. F. Dietrich, *Cancer Letters*, 2020, **470**, 204–219.
55 S.-G. Moslem, J. Soo and K. Hyock-Ju, *Nano Futures*, 2021, **5**(2), DOI: 10.1088/2399-1984/abfebc.
56 D. Qin, L. Zhang, H. Zhu, J. Chen, D. Wu, A. Bouakaz, M. Wan and Y. Feng, *Int. J. Nanomed.*, 2021, **16**, 3105–3119.
57 Y. Hadadian, J. H. Uliana, A. A. O. Carneiro and T. Z. Pavan, *IEEE Trans. Biomed. Eng.*, 2021, **68**, 68–77.
58 A. Milgroom, M. Intrator, K. Madhavan, L. Mazzaro, R. Shandas, B. Liu and D. Park, *Colloids Surf., B*, 2014, **116**, 652–657.
59 M. Guo, W. Du, N. Lyu, X. Chen, Y. Du, H. Wang, D. Yang, S. Wu, J. Liang and Y. Pan, *Adv. Healthcare Mater.*, 2020, **9**, 1901155.
60 R. A. Barmin, P. G. Rudakovskaya, O. I. Gusliakova, O. A. Sindeeva, E. S. Prikhozhdenko, E. A. Maksimova, E. N. Obukhova, V. S. Chernyshev, B. N. Khlebtsov and A. A. Solovev, *Nanomaterials*, 2021, **11**, 415.
61 L. G. Delogu, G. Vidili, E. Venturelli, C. Ménard-Moyon, M. A. Zoroddu, G. Pilo, P. Nicolussi, C. Ligios, D. Bedognetti and F. Sgarrella, *Proc. Natl. Acad. Sci. U. S. A.*, 2012, **109**, 16612–16617.
62 Y. Zhang, Y. Dong, H. Fu, H. Huang, Z. Wu, M. Zhao, X. Yang, Q. Guo, Y. Duan and Y. Sun, *Biomaterials*, 2020, 120478.
63 V. Schwarze, C. Marschner, G. N. de Figueiredo, J. Rübenthaler and D.-A. Clevert, *Eur. J. Ultrasound*, 2020, **41**, 29–35.
64 M. Bruce, A. Hannah, R. Hammond, Z. Z. Khaing, C. Tremblay-Darveau, P. N. Burns and C. P. Hofstetter, *IEEE Trans. Ultrason. Eng.*, 2020, **67**(9), 1776–1784.
65 W. K. Chong, V. Papadopoulou and P. A. Dayton, *Abdominal Radiol.*, 2018, **43**, 762–772.
66 A. L. Emanuel, R. I. Meijer, E. van Poelgeest, P. Spoor, E. H. Serné and E. C. Eringa, *Microcirculation*, 2020, **27**, e12588.
67 S. Turco, P. Frinking, R. Wildeboer, M. Arditi, H. Wijkstra, J. R. Lindner and M. Mischi, *Ultrasound Med. Biol.*, 2020, **46**(3), 518–543.
68 Z. Zhang, C. Huang, L. Zhang, Q. Guo, Y. Qin, F. Fan, B. Li, B. Xiao, D. Zhu and L. Zhang, *Acta Pharm. Sin. B*, 2020, **11**(2), 520–533.
69 K. G. Brown, D. Ghosh and K. Hoyt, *IEEE Trans. Ultrason. Eng.*, 2020, DOI: 10.1109/ULTSYM.2019.8926282.
70 R. R. Wildeboer, C. K. Mannaerts, R. J. van Sloun, L. Budäus, D. Tilki, H. Wijkstra, G. Salomon and M. Mischi, *Eur. Radiol.*, 2020, **30**, 806–815.
71 K. A. Stewart, S. M. Navarro, S. Kambala, G. Tan, R. Poondla, S. Lederman, K. Barbour and C. Lavy, *Int. J. MCH AIDS*, 2020, **9**, 103–120.
72 R. C. Wang, A. E. Kornblith, J. Grupp-Phelan, R. Smith-Bindman, L. S. Kao and J. Fahimi, *Am. J. Roentgenol.*, 2020, **216**, 200–208.
73 M. A. Averkiou, M. F. Bruce, J. E. Powers, P. S. Sheeran and P. N. Burns, *Ultrasound Med. Biol.*, 2020, **46**, 498–517.
74 V. Rafailidis, D. Y. Huang, G. T. Yusuf and P. S. Sidhu, *Ultrasonography*, 2020, **39**, 22.
75 A. Ajoolabady, A. Aghanejad, Y. Bi, Y. Zhang, H. Aslkhodapasandhukmabad, A. Abhari and J. Ren, *Biochim. Biophys. Acta Rev. Cancer*, 2020, **1874**(1), 188366.
76 H. W. West and C. Antoniades, *Antioxid. Redox Signa.*, 2020, **34**(15), 1217–1243.
77 Q. Jin, C.-Y. Lin, S.-T. Kang, Y.-C. Chang, H. Zheng, C.-M. Yang and C.-K. Yeh, *Ultrason. Sonochem.*, 2017, **36**, 262–269.
78 A. Luong, D. Smith, C.-H. Tai, B. Cotter, C. Luo, M. Strachan, A. DeMaria and J. J. Rychak, *Ultrasound Med. Biol.*, 2020, **46**, 690–702.
79 C. Lau, M. Rivas, J. Dinalo, K. King and V. Duddalwar, *J. Ultrasound Med.*, 2020, **39**, 19–28.
80 J. R. Eisenbrey and F. Forsberg, *Eur. J. Nucl. Med. Mol. Imaging*, 2010, **37**, 138–146.
81 R. Pala, S. Pattnaik, S. Busi and S. M. Nauli, *Pharmaceutics*, 2021, **13**(3), 348.
82 A. Rix, A. Curaj, E. Liehn and F. Kiessling, *Semin. Thromb. Hemost.*, 2020, **46**, 545–552.
83 G. Cismaru, T. Serban and A. Tirpe, *Biomedicines*, 2021, **9**(4), 418.
84 S. Feinstein and A. K. Rao, in *Therapeutic Lipidology*, ed. M. H. Davidson, P. P. Toth and K. C. Maki, Springer International Publishing, Cham, 2021, pp. 605–614, DOI: 10.1007/978-3-030-56514-5_32.
85 Q. Wang, F. Chan Kai, K. Schweizer, X. Du, D. Jin, H. Yu Simon Chun, J. Nelson Bradley and L. Zhang, *Sci. Adv.*, 2021, **7**(9), eabe5914.
86 S. Zhang, W. Chu, H. Wang, Y. Liang, Y. Fan, H. Liu and G. Wei, *J. Int. Med. Res.*, 2020, **48**, 0300060520942098.
87 W. Wu, X. Feng, Y. Yuan, Y. Liu, M. Li, J. Bin, Y. Xiao, W. Liao, Y. Liao and W. Zhang, *Mol. Imaging Biol.*, 2017, **19**, 183–193.
88 X. Leng, J. Wang, A. Carson, X. Chen, H. Fu, S. Ottoboni, W. R. Wagner and F. S. Villanueva, *Mol. Imaging*, 2014, **13**, 7290.
89 K. Thayse, N. Kindt, S. Laurent and S. Carlier, *Biology*, 2020, **9**(11), 368.
90 A. Rix, S. Fokong, S. Heringer, R. Pjontek, L. Kabelitz, B. Theek, M.-A. Brockmann, M. Wiesmann and F. Kiessling, *Invest. Radiol.*, 2016, **51**, 767–775.
91 K. E. Hitchcock, D. N. Caudell, J. T. Sutton, M. E. Klegerman, D. Vela, G. J. Pyne-Geithman, T. Abruzzo, P. E. Cyr, Y.-J. Geng and D. D. McPherson, *J. Controlled Release*, 2010, **144**, 288–295.
92 F. Moccetti, C. C. Weinkauf, B. P. Davidson, J. T. Belcik, E. R. Marinelli, E. Unger and J. R. Lindner, *Ultrasound Med. Biol.*, 2018, **44**, 1155–1163.
93 A. Maier, P. Plaza-Heck, F. Meixner, F. Guenther, B. A. Kaufmann, M. Kramer, T. Heidt, A. Zirlik, I. Hilgendorf and J. Reinöhl, *Atherosclerosis*, 2017, **267**, 68–77.
94 F. Chen, M. Ma, J. Wang, F. Wang, S.-X. Chern, E. R. Zhao, A. Jhunjhunwala, S. Darmadi, H. Chen and J. V. Jokerst, *Nanoscale*, 2017, **9**, 402–411.

95 V. Daeichin, K. Kooiman, I. Skachkov, J. G. Bosch, T. L. Theelen, K. Steiger, A. Needles, B. J. Janssen, M. J. Daemen and A. F. van der Steen, *Ultrasound Med. Biol.*, 2016, **42**, 2283–2293.
96 J. Lux, A. M. Vezeridis, K. Hoyt, S. R. Adams, A. M. Armstrong, S. R. Sirsi and R. F. Mattrey, *ACS Appl. Mater. Interfaces*, 2017, **9**, 37587–37596.
97 D. Myers, P. Lester, R. Adili, A. Hawley, L. Durham, V. Dunivant, G. Reynolds, K. Crego, Z. Zimmerman, S. Sood, R. Sigler, W. Fogler, J. Magnani, M. Holinstat and T. Wakefield, *J. Vasc. Surg.: Venous Lymphat. Disord.*, 2020, **8**, 268–278.
98 A. Yang, B. Qiao, E. M. Strohm, J. Cao, Z. Wang, X. Yuan, Y. Luo and Y. Sun, *Biomater. Sci.*, 2020, **8**, 4545–4558.
99 S. Wei, N. Fu, Y. Sun, Z. Yang, L. Lei, P. Huang and B. Yang, *Ultrasound Med. Biol.*, 2014, **40**, 1250–1259.
100 A. Ingels, I. Leguerney, P.-H. Cournède, J. Irani, S. Ferlicot, C. Sébrié, B. Benatsou, L. Jourdain, S. Pitre-Champagnat and J.-J. Patard, *Sci. Rep.*, 2020, **10**, 1–8.
101 X.-M. Guo, J.-L. Chen, B.-H. Zeng, J.-C. Lai, C.-Y. Lin and M.-Y. Lai, *RSC Adv.*, 2020, **10**, 39348–39358.
102 P. Li, L. Jin, L. Feng, Y. Wang and R. Yang, 2021, DOI: 10.21203/rs.3.rs-400253/v1.
103 M. Zhao, Y. Zhu, Y. Zhang, X. Yang, Y. Duan, Y. Chen and Y. Sun, *Clinical Hemorheology and Microcirculation*, 2020, pp. 1–11, Preprint.
104 H. Wu, H. Shi, H. Zhang, X. Wang, Y. Yang, C. Yu, C. Hao, J. Du, H. Hu and S. Yang, *Biomaterials*, 2014, **35**, 5369–5380.
105 L. J. Delaney, J. R. Eisenbrey, D. Brown, J. R. Brody, M. Jimbo, B. E. Oeffinger, M. Stanczak, F. Forsberg, J.-B. Liu and M. A. Wheatley, *Acta Biomater.*, 2021, **130**, 385–394.
106 K. Singh, D. S. Chopra, D. Singh and N. Singh, *Arabian J. Chem.*, 2020, **13**, 9034–9046.
107 S. V. Bachawal, K. C. Jensen, K. E. Wilson, L. Tian, A. M. Lutz and J. K. Willmann, *Cancer Res.*, 2015, **75**, 2501–2509.
108 R. Bam, P. S. Lown, L. A. Stern, K. Sharma, K. E. Wilson, G. R. Bean, A. M. Lutz, R. Paulmurugan, B. J. Hackel and J. Dahl, *Clin. Cancer Res.*, 2020, **26**, 2140–2150.
109 Y. Liu, Y. Zhou, J. Xu, H. Luo, Y. Zhu, X. Zeng, F. Dong, Z. Wei, F. Yan and H. Zheng, *Biomater. Sci.*, 2021, **9**, 2454–2466.
110 L. Xu, J. Du, C. Wan, Y. Zhang, S. Xie, H. Li, H. Yang and F. Li, *Int. J. Nanomed.*, 2018, **13**, 1791.
111 D. Sheng, L. Deng, P. Li, Z. Wang and Q. Zhang, *ACS Biomater. Sci. Eng.*, 2021, **7**, 605–616.
112 X. Z. Li, J. Song, Z. X. Sun, Y. Y. Yang, Y. Q. Lin and H. Wang, *J. Ultrasound Med.*, 2020, **39**(9), 1687–1694.
113 T. Zhou, W. Cai, H. Yang, H. Zhang, M. Hao, L. Yuan, J. Liu, L. Zhang, Y. Yang and X. Liu, *J. Controlled Release*, 2018, **276**, 113–124.
114 B. Shang, X. Zhang, R. Ji, Y. Wang, H. Hu, B. Peng and Z. Deng, *Mater. Sci. Eng.: C*, 2020, **106**, 110174.
115 J.-P. Wang, X.-L. Zhou, J.-P. Yan, R.-Q. Zheng and W. Wang, *Oncotarget*, 2017, **8**, 78153.
116 Y. Gao, C. Hernandez, H.-X. Yuan, J. Lilly, P. Kota, H. Zhou, H. Wu and A. A. Exner, *Nanomedicine*, 2017, **13**, 2159–2168.
117 Y. Zhang, Y. Dong, H. Fu, H. Huang, Z. Wu, M. Zhao, X. Yang, Q. Guo, Y. Duan and Y. Sun, *Biomaterials*, 2021, **269**, 120478.
118 H. Zhou, J. Fu, Q. Fu, Y. Feng, R. Hong, P. Li, Z. Wang, X. Huang and F. Li, *PeerJ*, 2021, **9**, e11486.
119 X. Duan and M. Hou, *Revista Cientifica-Facultad de Ciencias Veterinarias*, 2020, **30**(1), 320–330.
120 Q. Dongying, L. Lan and D. Qian, *Process Biochem.*, 2020, **98**, 51–58.
121 Y. Liu, J. Jiang, C. Liu, W. Zhao, Y. Ma, Z. Zheng, Q. Zhou and Y. Zhao, *Am. J. Transl. Res.*, 2021, **13**, 988–1005.
122 Q. Hu, X.-Y. Wang, L.-K. Kang, H.-M. Wei, C.-M. Xu, T. Wang and Z.-H. Wen, *PLoS One*, 2016, **11**, e0149075.
123 H. Wang, S. A. Felt, S. Machtaler, I. Guracar, R. Luong, T. Bettinger, L. Tian, A. M. Lutz and J. K. Willmann, *Radiology*, 2015, **276**, 809–817.
124 T. Payen, A. Dizeux, C. Baldini, D. Le Guillou-Buffello, M. Lamuraglia, E. Comperat, O. Lucidarme and S. L. Bridal, *Ultrasound Med. Biol.*, 2015, **41**, 2202–2211.
125 J. Zhu, Z. Wang, X. Xu, M. Xu, X. Yang, C. Zhang, J. Liu, F. Zhang, X. Shuai and W. Wang, *Mol. Pharmaceutics*, 2020, **17**, 817–826.
126 A. Helbert, M. Von Wronski, D. Colevret, C. Botteron, F. Padilla, T. Bettinger, I. Tardy and J.-M. Hyvelin, *Invest. Radiol.*, 2020, **55**(10), 657–665.
127 C. Qiu, T. Sha, T. Yin, W. Zhang, X. Chen, X. Miao, R. Zheng, X. Shuai and J. Ren, *Biomater. Sci.*, 2021, **9**(17), 5802–5811.
128 Q. Wu, Q. Zhang, T. Yu, X. Wang, C. Jia, Z. Zhao and J. Zhao, *ACS Appl. Bio Mater.*, 2021, **4**, 4244–4253.
129 N. Shimamoto, M. Ito, M. Chiba, S. Honma, H. Imazu and K. Sumiyama, *Hepatobil. Pancreat. Dis. Int.*, 2020, **19**, 478–485.
130 M. Lamuraglia, G. Barrois, D. Le Guillou-Buffello, M. Santin, A. Kerbol, E. Comperat, A. Coron, O. Lucidarme and S. L. Bridal, *Technol. Cancer Res. Treat.*, 2020, **19**, 1533033819886896.
131 R. Bam, I. Daryaei, L. Abou-Elkacem, J. G. Vilches-Moure, E. J. Meuillet, A. Lutz, E. R. Marinelli, E. C. Unger, S. S. Gambhir and R. Paulmurugan, *Invest. Radiol.*, 2020, **55**(11), 711–721.
132 G. Köse, M. Darguzyte and F. Kiessling, *Nanomaterials*, 2020, **10**(10), 1935.
133 R. H. Perera, X. Wang, Y. Wang, G. Ramamurthy, P. Peiris, E. Abenojar, J. P. Basilion and A. A. Exner, *Nanomedicine*, 2020, **28**, 102213.
134 E. Heer, A. Harper, N. Escandor, H. Sung, V. McCormack and M. M. Fidler-Benaoudia, *Lancet Global Health*, 2020, **8**, e1027–e1037.
135 A. A. Berlin, M. Young, A. E. Kaffas, S. Gambhir, A. Lutz, M. L. Storto and J. Willmann, 2020, arXiv preprint arXiv:2006.11993.
136 Y. Zhang, Y. Li, M. Wu, F. Zhang, G. Shao and Q. Wang, *J. Med. Imaging Health Inform.*, 2021, **11**, 981–987.

137 A. Tarighatnia, M. H. Abdkarimi, N. D. Nader, T. Mehdipour, M. R. Fouladi, A. Aghanejad and H. Ghadiri, *New J. Chem.*, 2021, **45**, 18871–18880.
138 P. Tomà, *Pediatr. Radiol.*, 2020, **50**, 314–320.
139 M. A. Zamzam, A. A. Abd El-Aziz, I. I. El-Mahallway, G. A. AbdeLaal, M. K. Abd El-Mageed and H. A. Eid, *Egyptian J. Chest Dis. Tuberculos.*, 2020, **69**, 183.
140 X. Yu, Y. Yang and J. Li, *Eur. J. Inflamm.*, 2020, **18**, 2058739220961194.
141 Y. Wu, T. Sun, J. Tang, Y. Liu and F. Li, *Ultrasound Med. Biol.*, 2020, **46**, 679–689.
142 M. B. Toaldo, V. Salvatore, S. Marinelli, C. Palamà, M. Milazzo, L. Croci, L. Venerandi, M. Cipone, L. Bolondi and F. Piscaglia, *Mol. Imaging Biol.*, 2015, **17**, 29–37.
143 L. Barghi, A. Aghanejad, H. Valizadeh, J. Barar and D. Asgari, *Adv. Pharm. Bull*, 2012, **2**(1), 119–122.
144 D. Asgari, A. Aghanejad and J. S. Mojarrad, *Bull. Korean Chem. Soc.*, 2011, **32**, 909–914.